Transient temperature distribution in a multilayer semiconductor device with dynamic thermal load and non-uniform thermal contact resistance between layers

Girish Krishnan, Ankur Jain*

Mechanical and Aerospace Engineering Department, University of Texas at Arlington, Arlington, TX, USA

ABSTRACT

The thermal management challenge in microelectronic chips is exacerbated by their multilayer architecture and manufacturing processes that introduce non-uniform thermal contact resistance between adjacent layers. Most of the past work on development of thermal models to predict temperature distribution in microelectronic chips either does not account for such thermal contact resistance at all, or simply assumes it to be spatially uniform. This work presents an exact analytical solution for the transient temperature distribution in a multilayer chip with non-uniform thermal contact resistance between layers as well as dynamic, non-uniform heat generation. The problem is solved by first carrying out a Laplace transformation and then implementing a series solution, the coefficients of which are determined by solving a set of algebraic equations derived from the non-uniform thermal contact resistances between adjacent layers. While the problem is solved for a general *M*-layered chip, the solution for the practical case of a two-layer chip is also provided. Results indicate that the temperature distribution and its evolution over time is determined by the nature of the non-linear thermal contact resistance, and its overlap with the dynamic heat loads imposed on the chip. The impact of these and other relevant parameters is examined in detail. Results presented here improve the fundamental understanding of thermal transport modeling in multilayer semiconductor chips, with possible applications in other multilayer engineering systems as well.

© 2023 Elsevier Ltd. All rights reserved.

1. Introduction

Thermal management of microelectronic devices remains a long-standing technological challenge [1,2]. Heat generation during device operation, for example, due to transistor switching or current flow through a resistive interconnect must be adequately dissipated in order to avoid performance reduction and reliability problems at elevated temperature [1,2]. Examples of heat removal technologies in microelectronic devices and systems range from air cooling with the aid of heat sinks for relatively low power chips [2–5] to heat pipes [4], vapor chambers [6], immersion cooling [7] and related technologies for high power chips. The increase in device density with successive technology nodes and the introduction of new architectures and packaging technologies continues to exacerbate the thermal management challenge [8–10]. Thermal management is particularly challenging for multilayer semiconductor architectures such as three-dimensional integrated circuits (3D ICs) [11] where heat generation in multiple parallel transistor layers results in overlap of heat maps. Moreover, the limited thermal access to intermediate layers in a 3D IC makes heat removal even more challenging.

A considerable amount of literature already exists on experimental and theoretical investigation of thermal management of 3D ICs. A number of experimental methods for cooling of 3D ICs have been reported. Some of these include single and two-phase liquid cooling [8,9], thermal management using TSVs [8,12,13] and cooling through air gaps [8]. On the other hand, available theoretical models for heat transfer in 3D ICs include thermal resistance network based models [1], detailed analytical models [14–16], numerical models [17,18] and coupled thermal-electrical models [19]. Algorithms to integrate thermal modeling within various aspects of the 3D IC design process, including thermally aware floorplanning [20,21], via placement [22], routing [23] and performance analysis [24] have been reported. Thermomechanical simulations to predict and minimize the undesirable effect of thermomechanical stress in the vicinity of a through-Silicon via (TSV) have also been reported [25].

Similar to other semiconductor devices, spatial distributions of heat generation, or power maps on a 3D IC are highly dynamic,

---

* Corresponding author.
  E-mail address: jaina@uta.edu (A. Jain).

Nomenclature

Bi	Biot number, $Bi = \frac{hz_M}{k_M}$
$\bar{g}$	non-dimensional thermal contact resistance, $\bar{g}_m(\eta) = \frac{R_m(y)k_M}{z_M}$
h	convective heat transfer coefficient (Wm^{-2}K^{-1})
k	thermal conductivity (Wm^{-1}K^{-1})
$\bar{k}$	non-dimensional thermal conductivity, $\bar{k}_m = \frac{k_m}{k_M}$
M	number of layers
N	number of eigenvalues
q''	heat flux (Wm^{-2})
$\bar{q}$	non-dimensional heat flux, $\bar{q}(\eta) = \frac{q''(y)z_M}{k_M(T_{ref}-T_{amb})}$
$\hat{q}$	Laplace transform of the heat flux
R	spatially varying thermal contact resistance (Km^{2}W^{-1})
s	Laplace variable
T	temperature (K)
θ	non-dimensional temperature, $\theta_m = \frac{T_m-T_{amb}}{T_{ref}-T_{amb}}$
t	time (s)
w	width in the y direction (m)
$\bar{w}$	non-dimensional width in the y direction, $\bar{w} = \frac{w}{z_M}$
y, z	spatial coordinates (m)
α	diffusivity (m^{2}s^{-1})
$\bar{\alpha}$	non-dimensional diffusivity, $\bar{\alpha}_m = \frac{\alpha_m}{\alpha_M}$
γ	non-dimensional interface location, $\gamma_m = \frac{x_m}{z_M}$
λ	non-dimensional eigenvalue in η direction
η, ξ	non-dimensional spatial coordinates, $\eta = \frac{y}{z_M}$; $\xi = \frac{z}{z_M}$
$\hat{\theta}$	Laplace transform of the temperature field
τ	non-dimensional time, $\tau = \frac{\alpha_M t}{z_M^2}$

Subscripts

amb	ambient
m	layer number
ref	reference
in	initial

depending on how the various components of a highly heterogeneous architecture are being used over time. While the simplest 3D IC thermal models are steady state in nature [26,27], transient models that account for such dynamic heat generation have also been reported [28].

A key feature of much consequence to thermal management that is somewhat unique to 3D ICs is the thermal contact resistance between adjacent layers. In a non-monolithic 3D IC, individual layers are fabricated separately and bonded to each other through a variety of techniques such as dielectric bonding [29] and metal bonding [30]. Most commonly, bond pads on the mating surfaces of two die/wafers are aligned and pressed against each other at high temperature and pressure, resulting in bonding mediated by the formation of intermetallic eutectics in the bond pads [30]. From a heat transfer perspective, such bonding is never thermally perfect, and, therefore, introduces a thermal contact resistance between layers that depends strongly on the nature of the bonding process and the bond pad materials. Moreover, a large fraction of the mating surface does not contain bond pads, and, therefore, such vacant space also contributes towards thermal resistance. Limited experimental measurements of such inter-layer thermal contact resistance indicate values in the range of 10^{-5} Km^2/W [17,31], which clearly indicates the importance of modeling such contact resistance when computing or simulating the temperature field in the 3D IC.

Since such bond pads also facilitate electrical interconnection between layers, therefore, the density of such bond pads is not uniform throughout the mating surface. For example, bond pads with larger size and area density are designed in regions that require extensive interconnection between layers. Bond pads and TSVs must also compete with other components for a limited available space during the floorplanning process.

The discussion above clearly implies that thermal contact resistance between adjacent layers in a 3D IC is spatially distributed instead of being uniform. In conjunction with the heat load on each layer that varies with time, this presents a significant challenge in thermal modeling of a multilayer 3D IC. While thermal models with dynamic heat load are commonly available in the literature [1], the modeling of thermal contact resistances between layers is either absent altogether, or, at best, is modeled only as uniform. In order to minimize errors that may arise from such approximations, there is clearly a need for thermal modeling that accounts for both dynamic heat load as well as spatially varying thermal contact resistances between layers. Some literature is available on the modeling of spatially varying interfacial thermal contact resistance or convective heat transfer coefficient at a boundary [15,32]. However, such models are typically steady state in nature, and extension to transient analysis is of much importance in order to account for the dynamic nature of heat generation in a 3D IC.

This work presents Laplace transform based analysis of transient thermal conduction in a multilayer 3D IC with dynamic, non-uniform heat generation and spatially distributed thermal contact resistance between layers. Analysis is presented for a general *M*-layer geometry with results also presented for a special case of two-layer 3D IC. Closed form expressions for the temperature field in the Laplace domain are derived in the form of eigenfunction-based infinite series, the coefficients of which are determined by solving a set of algebraic equations derived from the spatial variation of heat flux and thermal contact resistance. Results indicate that the interaction between the dynamic heat load and spatially varying thermal contact resistance determines the nature of the temperature field. Results derived in this work are expected to aid the thermal design of 3D ICs and other multilayer structures with significant contact resistance, towards improved performance and reliability.

The key novelty of the present work is in developing an analytical model to compute the transient temperature distribution in a multilayer body, accounting for spatially varying contact resistance between layers, which is a realistic condition encountered in 3D ICs. The transient temperature distribution derived here can not be determined by a straightforward extension of past work, which either is limited to steady state [15], treats the contact resistance as constant [16] or does not account for contact resistance at all [33]. Solving the transient problem defined here necessitates developing and solving a transient thermal model, which is the key contribution of the present work.

2. Problem definition

Fig. 1(a) depicts the schematic of the *M*-layer semiconductor device of width w being considered in this work. Analysis is presented here for a 2D chip for mathematical simplicity, although extension to a 3D geometry is straightforward. In general, each layer may be a distinct material, with given thermal properties. The sidewalls are assumed to be adiabatic, which is justified due to the relatively small thickness of the semiconductor chip, which results in minimal heat loss from the sides. Additionally, modern microprocessor chips usually have multiple cores and other functional blocks, resulting in spatially varying, dynamic hotspots depending on the workload. In order to model this, a dynamically switching and spatially varying heat load $q''(y,t)$ is assumed on the bottom
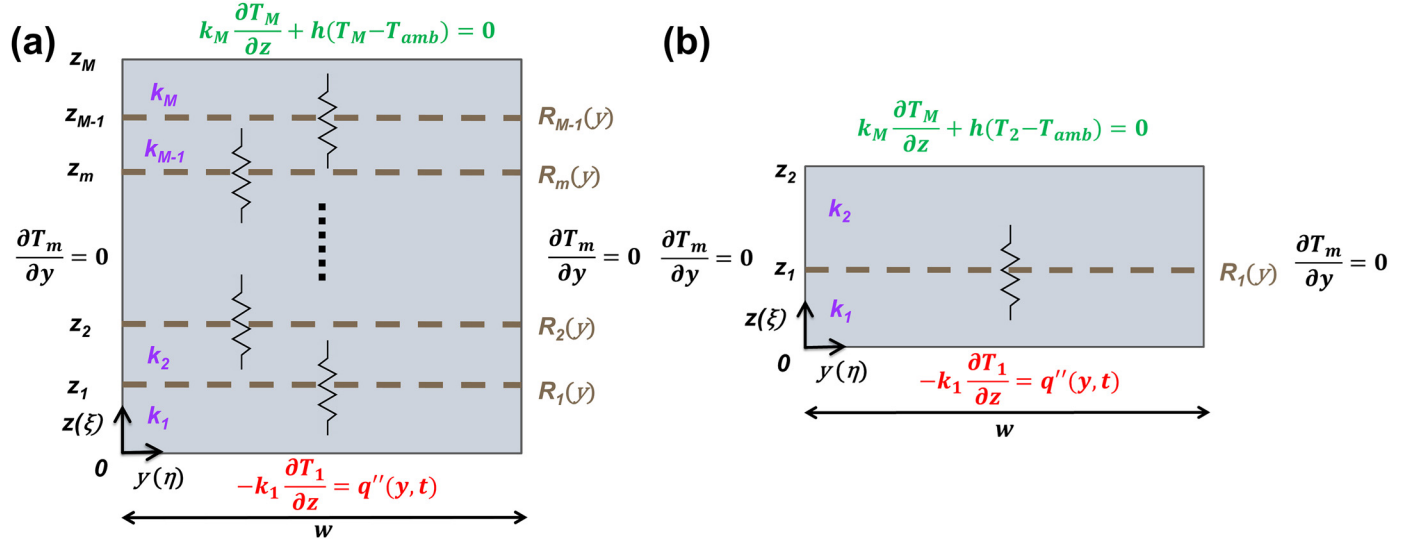
Fig. 1. Schematics of (a) a general M-layer semiconductor device and (b) the specific case of a two-layer semiconductor device.

face of the geometry. It is reasonable to model this as a boundary condition since heat generation in a typical semiconductor device occurs in a very thin region at the top of the substrate. Heat generation in only one plane is modeled here, since, based on linearity of this problem, the effects of heat generation in multiple planes can be computed separately and simply added linearly. The multilayer device is assumed to be convectively cooled on the top surface, modeled by a constant and uniform convective heat transfer coefficient h. The bottom and top faces are referred to as the heat flux face and heat dissipation face, respectively. The total thickness of the multilayer body is z_M, with the thickness of the mth layer being $z_m - z_{m-1}$. As shown in Fig. 1(a), in order to model the spatially varying nature of bonding between adjacent die, a thermal contact resistance $R_m(y)$ is assumed at the interface between $(m-1)^{th}$ and m^{th} die.

The interest here is to derive expressions for the transient temperature distribution in the M-layer body, and specifically to understand the impact of the dynamically varying heat load $q(y,t)$ and thermal contact resistance $R_m(y)$ on the thermal performance of the device. Based on the problem definition above, the following governing energy conservation equations for each layer and boundary conditions may be written

$$\alpha_m\left(\frac{\partial^2 T_m}{\partial y^2} + \frac{\partial^2 T_m}{\partial z^2}\right) = \frac{\partial T_m}{\partial t} \qquad (m = 1, 2..M) \quad (1)$$

$$-k_1\frac{\partial T_1}{\partial z} = q''(y,t) (z = 0) \quad (2)$$

$$k_M\frac{\partial T_M}{\partial z} + h(T_M - T_{amb}) = 0 \quad (z = z_M) \quad (3)$$

$$\frac{\partial T_m}{\partial y} = 0 (y = 0, w) \quad (4)$$

Based on the spatially varying thermal contact resistance, the interface conditions are given by

$$T_m = T_{m+1} - k_m\frac{\partial T_m}{\partial z}R_m(y) (z = z_m) \qquad (m = 1, 2..M - 1) \quad (5)$$

$$k_m\frac{\partial T_m}{\partial z} = k_{m+1}\frac{\partial T_{m+1}}{\partial z} (z = z_m) \qquad (m = 1, 2..M - 1) \quad (6)$$

Finally, the initial condition for the problem is given by

$$T_m = T_{m,in} (t = 0) \qquad (m = 1, 2..M - 1) \quad (7)$$

where $T_{m,in}$ is a uniform initial temperature that the device is at prior to the onset of heat dissipation.

Non-dimensionalization for this problem is carried out using the following scheme:.

$$\theta_m = \frac{T_m - T_{amb}}{T_{ref} - T_{amb}}, \ \xi = \frac{z}{z_M}, \ \eta = \frac{y}{z_M}, \ \tau = \frac{\alpha_M t}{z_M^2}, \ \gamma_m = \frac{z_m}{z_M}, \bar{w}$$

$$= \frac{w}{z_M}, \bar{k}_m = \frac{k_m}{k_M}, \bar{\alpha}_m = \frac{\alpha_m}{\alpha_M}, \theta_{m,in} = \frac{T_{m,in} - T_{amb}}{T_{ref} - T_{amb}}, \bar{q}(\eta, \tau)$$

$$= \frac{q''(y,t)z_M}{k_M(T_{ref} - T_{amb})}, \bar{g}_m(\eta) = \frac{R_m(y)k_M}{z_M}, Bi = \frac{hz_M}{k_M} \quad (8)$$

where T_{ref} is a reference temperature.

Based on this, the following set of non-dimensional equations may be written:

$$\bar{\alpha}_m\left(\frac{\partial^2\theta_m}{\partial\xi^2} + \frac{\partial^2\theta_m}{\partial\eta^2}\right) = \frac{\partial\theta_m}{\partial\tau} \qquad (m = 1, 2..M) \quad (9)$$

$$-\bar{k}_1\frac{\partial\theta_1}{\partial\xi} = \bar{q}(\eta, \tau) \quad (\xi = 0) \quad (10)$$

$$\bar{k}_M\frac{\partial\theta_M}{\partial\xi} + Bi \cdot \theta_M = 0 \quad (\xi = 1) \quad (11)$$

$$\frac{\partial\theta_m}{\partial\eta} = 0 \quad (\eta = 0, \ \bar{w}) \qquad (m = 1, 2..M) \quad (12)$$

$$\theta_m = \theta_{m+1} - \bar{k}_m\frac{\partial\theta_m}{\partial\xi}\bar{g}_m(\eta) \ (\xi = \gamma_m) \qquad (m = 1, 2..M - 1) \quad (13)$$

$$\bar{k}_m\frac{\partial\theta_m}{\partial\xi} = \bar{k}_{m+1}\frac{\partial\theta_{m+1}}{\partial\xi} \ (\xi = \gamma_m) \qquad (m = 1, 2..M - 1) \quad (14)$$

$$\theta_m = \theta_{m,in} \quad (\tau = 0) \qquad (m = 1, 2..M) \quad (15)$$

The existence of a general dynamically switching and spatially varying heat load precludes the use of separation of variables technique for solving this problem. Instead, a solution is derived in the Laplace domain. Laplace transformation of Eqs. (9)–(14), along with the use of the initial condition from Eq. (15) results in the following governing equation and boundary conditions in the Laplace domain.

$$\bar{\alpha}_m\left(\frac{\partial^2\hat{\theta}_m}{\partial\xi^2} + \frac{\partial^2\hat{\theta}_m}{\partial\eta^2}\right) = s\hat{\theta}_m - \theta_{m,in} \qquad (m = 1, 2, 3...M) \quad (16)$$

$$-\bar{k}_1 \frac{\partial \hat{\theta}_1}{\partial \xi} = \hat{q}(\eta, s)(\xi = 0) \tag{17}$$

$$\frac{\partial \hat{\theta}_M}{\partial \xi} + Bi\hat{\theta}_M = 0 \quad (\xi = 1) \tag{18}$$

$$\frac{\partial \hat{\theta}_m}{\partial \eta} = 0 \quad (\eta = 0, \ \bar{w}) \qquad (m = 1, 2..M) \tag{19}$$

$$\hat{\theta}_m = \hat{\theta}_{m+1} - \bar{k}_m \frac{\partial \hat{\theta}_m}{\partial \xi} \bar{g}_m(\eta) \quad (\xi = \gamma_m) \quad (m = 1, 2..M - 1) \tag{20}$$

$$\bar{k}_m \frac{\partial \hat{\theta}_m}{\partial \xi} = \bar{k}_{m+1} \frac{\partial \hat{\theta}_{m+1}}{\partial \xi} \quad (\xi = \gamma_m) \qquad (m = 1, 2..M - 1) \tag{21}$$

In the equations above, $\hat{\theta}_m$ and $\hat{q}$ are the temperature field and heat flux, respectively, in the Laplace domain and s is the Laplace variable.

In order to solve this set of equations, a transformation is first carried out as follows

$$\hat{\theta}_m = \hat{u}_m(\eta) + \hat{\phi}_m(\xi, \eta) \tag{22}$$

This transformation, when used in Eq. (16) results in two inter-linked problems. The first problem in $\hat{u}_m(\eta)$ may be written as:

$$\bar{\alpha}_m \frac{d^2\hat{u}_m}{d\eta^2} = s\hat{u}_m - \theta_{m,in} \tag{23}$$

subject to

$$\frac{d\hat{u}_m}{d\eta} = 0 \quad (\eta = 0, \ \bar{w}) \tag{24}$$

A solution for $\hat{u}_m(\eta)$ is given by

$$\hat{u}_m(\eta) = \frac{\theta_{m,in}}{s} \tag{25}$$

On the other hand, the $\hat{\phi}_m(\xi, \eta)$ problem is given by

$$\bar{\alpha}_m \left(\frac{\partial^2 \hat{\phi}_m}{\partial \xi^2} + \frac{\partial^2 \hat{\phi}_m}{\partial \eta^2} \right) = s\hat{\phi}_m \qquad (m = 1, 2..M) \tag{26}$$

$$-\bar{k}_1 \frac{\partial \hat{\phi}_1}{\partial \xi} = \hat{q}(\eta, s)(\xi = 0) \tag{27}$$

$$\frac{\partial \hat{\phi}_M}{\partial \xi} + Bi\hat{\phi}_M = -Bi\hat{u}_M(\eta) \quad (\xi = 1) \tag{28}$$

$$\frac{\partial \hat{\phi}_m}{\partial \eta} = 0 \quad (\eta = 0, \ \bar{w}) \qquad (m = 1, 2..M) \tag{29}$$

$$\hat{\phi}_m + \hat{u}_m(\eta) = \hat{\phi}_{m+1} + \hat{u}_{m+1}(\eta) - \bar{k}_m \frac{\partial \hat{\phi}_m}{\partial \xi} \bar{g}_m(\eta) \quad (\xi = \gamma_m)$$
$$(m = 1, 2..M - 1) \tag{30}$$

$$\bar{k}_m \frac{\partial \hat{\phi}_m}{\partial \xi} = \bar{k}_{m+1} \frac{\partial \hat{\phi}_{m+1}}{\partial \xi} \quad (\xi = \gamma_m) \qquad (m = 1, 2..M - 1) \tag{31}$$

A solution for Eq. (26) may be written as follows:

$$\hat{\phi}_m(\xi, \eta) = \sum_{n=0}^{N} (A_{m,n} \cosh(\omega_{m,n}\xi) + B_{m,n} \sinh(\omega_{m,n}\xi)) \cos(\lambda_n \eta)$$
$$(m = 1, 2..M) \tag{32}$$

where, using the governing equations, it can be shown that $\omega_{m,n} = \sqrt{\lambda_n^2 + \frac{s}{\alpha_m}}$.

In Eq. (32), the sine term is not considered based on the adiabatic boundary condition at $\eta = 0$, and the η-direction eigenvalues $\lambda_n = \frac{n\pi}{\bar{w}}$ are obtained using the boundary condition at $\eta = \bar{w}$. The

solution for $\hat{\phi}_m$ given by Eq. (32) involves $2(N + 1)M$ unknowns - $A_{m,n}$ and $B_{m,n}$. Boundary conditions and interface conditions along the layered direction are used one by one in order to derive a set of $2(N + 1)M$ linear algebraic equations, from which, these unknowns may be determined in order to complete the solution of the problem. By inserting the form of the solution for $\hat{\phi}_m$ given by Eq. (32) in Eq. (27), one may write

$$\sum_{n=0}^{N} \left(-\bar{k}_1 \omega_{1,n} B_{1,n} \right) \cos(\lambda_n \eta) = \hat{q}(\eta, s) \tag{33}$$

Multiplying Eq. (33) with $\cos(\lambda_{n'}\eta)$, where $n' = 0, 1, 2, .., N$ and integrating from $\eta = 0$ to $\eta = \bar{w}$ results in a total of $N + 1$ equations as follows:

$$N_{n'} \left(-\bar{k}_1 \omega_{1,n} B_{1,n} \right) = \int_0^{\bar{w}} \hat{q}(\eta, s) \cos(\lambda_{n'} \eta) d\eta \left(n' = 0, 1, 2, .., N \right) \tag{34}$$

where $N_{n'} = \int_0^{\bar{w}} \cos^2(\lambda_{n'}\eta) d\eta$.

The next $N + 1$ equations are obtained by a similar treatment of Eq. (28), resulting in

$$N_{n'}[(Bi \cosh(\omega_{M,n'}) + \omega_{M,n'} \sinh(\omega_{M,n'}))A_{M,n'} + (Bi \sinh(\omega_{M,n'})$$
$$+ \omega_{M,n'} \cosh(\omega_{M,n'}))B_{M,n'}]$$
$$= -Bi \int_0^{\bar{w}} \cos(\lambda_{n'}\eta) \hat{u}_M(\eta) d\eta \qquad (n' = 0, 1, 2, .., N) \tag{35}$$

Finally, the remaining $2(N + 1)(M-1)$ equations are derived from interface conditions given by Eqs. (30) and (31). The use of Eq. (32) in these equations, followed by multiplication with $\cos(\lambda_{n'}\eta)$ and integration from $\eta = 0$ to $\eta = \bar{w}$ results in

$$N_{n'}(A_{m,n'} \cosh(\omega_{m,n'}\gamma_m) + B_{m,n'} \sinh(\omega_{m,n'}\gamma_m))$$
$$= N_{n'}(A_{m+1,n'} \cosh(\omega_{m+1,n'}\gamma_m) + B_{m+1,n'} \sinh(\omega_{m+1,n'}\gamma_m))$$
$$+ \int_0^{\bar{w}} (\hat{u}_{m+1}(\eta) - \hat{u}_m(\eta)) \cos(\lambda_{n'}\eta) d\eta$$
$$- \sum_{n=0}^{N} \bar{k}_m \omega_{m,n}(A_{m,n} \sinh(\omega_{m,n}\gamma_m) + B_{m,n} \cosh(\omega_{m,n}\gamma_m))$$
$$\times \int_0^{\bar{w}} \bar{g}_m(\eta) \cos(\lambda_n \eta) \cos(\lambda_{n'}\eta) d\eta \qquad (n' = 0, 1, 2, .., N) \tag{36}$$

and

$$\bar{k}_m \omega_{m,n'}(A_{m,n'} \sinh(\omega_{m,n'}\gamma_m) + B_{m,n'} \cosh(\omega_{m,n'}\gamma_m))N_{n'}$$
$$= \bar{k}_{m+1}\omega_{m+1,n'}(A_{m+1,n'} \sinh(\omega_{m+1,n'}\gamma_m)$$
$$+ B_{m+1,n'} \cosh(\omega_{m+1,n'}\gamma_m))N_{n'} \qquad (n' = 0, 1, 2, .., N) \tag{37}$$

Eqs. (34)–(37) represent a sufficient set of linear equations in unknowns $A_{m,n}$ and $B_{m,n}$ $(n = 0, 1, 2, .., N; \ m = 1, 2..M)$. These equations are easily solved computationally to complete the solution of the problem in the Laplace domain. Inverse Laplace transformation of this solution is carried out numerically to determine the solution for $\theta(\xi, \eta, \tau)$. While a number of inversion algorithms are available [34–36], the present work utilizes Hollenbeck's algorithm [34].

3. Special case – two-layer body

The special case of a two-layer 3D IC, shown schematically in Fig. 1(b) is of particular interest due to its appearance in practical

problems, as well as its relevance for several past papers on multilayer two-dimensional heat transfer problems [15,33]. This section summarizes the solution for the two-layer problem, based on the solution methodology discussed in the previous section. In this case, the temperature fields of layers 1 and 2 in the Laplace domain are given by:

$$
\hat{\theta}_1(\xi, \eta) = \frac{\theta_{1,in}}{s} + \sum_{n=0}^{n=N} (A_{1,n} \cosh(\omega_{1,n}\xi) + B_{1,n} \sinh(\omega_{1,n}\xi)) \cos(\lambda_n \eta) \tag{38}
$$

$$
\hat{\theta}_2(\xi, \eta) = \frac{\theta_{2,in}}{s} + \sum_{n=0}^{n=N} (A_{2,n} \cosh(\omega_{2,n}(1-\xi)) + B_{2,n} \sinh(\omega_{2,n}(1-\xi))) \cos(\lambda_n \eta) \tag{39}
$$

where

$$
B_{1,n} = \frac{-\int_0^{\bar{w}} \hat{q}(\eta, s) \cos(\lambda_n \eta) d\eta}{\bar{k}_1 \omega_{1,n} N_n} \tag{40}
$$

$$
B_{2,n} = \frac{Bi\left[N_n A_{2,n} + \int_0^{\bar{w}} \hat{u}_2(\eta) \cos(\lambda_n \eta) d\eta \right]}{\omega_{2,n} N_n} \tag{41}
$$

Further, the $2(N+1)$ unknowns $A_{1,n}$ and $A_{2,n}$ $(n = 0, 1, 2, .., N)$ may be derived from the following set of linear equations:

$$
N_{n'} \bigg(A_{1,n'} \left[\bar{k}_1 \omega_{1,n'} \sinh(\omega_{1,n'} \gamma_1) \right]
$$
$$
+ A_{2,n'} [\omega_{2,n'} \sinh(\omega_{2,n'}(1-\gamma_1)) + Bi \cosh(\omega_{2,n'}(1-\gamma_1))]
$$
$$
+ \frac{Bi \cosh(\omega_{2,n'}(1-\gamma_1)) \int_0^{\bar{w}} \hat{u}_2(\eta) \cos(\lambda_{n'}\eta) d\eta}{N_{n'}}
$$
$$
- \frac{\cosh(\omega_{1,n'}\gamma_1) \int_0^{\bar{w}} \hat{q}(\eta, s) \cos(\lambda_{n'}\eta) d\eta}{N_{n'}} \bigg) = 0 \tag{42}
$$

$$
A_{1,n'} \left[N_{n'} \cosh(\omega_{1,n'}\gamma_1) \right]
$$
$$
+ \sum_{n=0}^{N} A_{1,n} \bar{k}_1 \omega_{1,n} \sinh(\omega_{1,n}\gamma_1) \int_0^{\bar{w}} \bar{g}_1(\eta) \cos(\lambda_n \eta) \cos(\lambda_{n'}\eta) d\eta
$$
$$
+ A_{2,n'} \left[-N_{n'} \cosh(\omega_{2,n'}(1-\gamma_1)) - \frac{Bi N_{n'}}{\omega_{2,n'}} \sinh(\omega_{2,n'}(1-\gamma_1)) \right]
$$
$$
= \int_0^{\bar{w}} \cos(\lambda_{n'}\eta) (\hat{u}_2(\eta) - \hat{u}_1(\eta)) d\eta
$$
$$
+ \frac{Bi \sinh(\omega_{2,n'}(1-\gamma_1)) \int_0^{\bar{w}} \hat{u}_2(\eta) \cos(\lambda_{n'}\eta) d\eta}{\omega_{2,n'}}
$$
$$
+ \frac{\sinh(\omega_{1,n'}\gamma_1) \int_0^{\bar{w}} \hat{q}(\eta, s) \cos(\lambda_{n'}\eta) d\eta}{\bar{k}_1 \omega_{1,n'}} \tag{43}
$$
$$
+ \sum_{n=0}^{N} \frac{\cosh(\omega_{1,n}\gamma_1) \int_0^{\bar{w}} \hat{q}(\eta, s) \cos(\lambda_n \eta) d\eta}{N_n}
$$
$$
\times \int_0^{\bar{w}} \bar{g}_1(\eta) \cos(\lambda_n \eta) \cos(\lambda_{n'}\eta) d\eta
$$

where both Eqs. (42) and (43) may be written for $n' = 0, 1, 2, \ldots N$.

4. Results and discussion

4.1. Convergence of the infinite series solution

Since the present work derives a system of linear equations in the Laplace domain, it is important to test for convergence. For a given number of layers, the number of terms considered in series,

N governs convergence. Based on this, Fig. 2 illustrates the impact of N on the computed temperature distribution. For this analysis, the representative heat load $\bar{q}$ at $\xi=0$ is initially constant with a magnitude of 1.0 until $\tau=0.4$. At $\tau=0.4$, the magnitude of heat load doubles between $\eta=0.4\bar{w}$ and $\eta=0.6\bar{w}$, thereby creating a hotspot. The thermal contact resistance $\bar{g}_1$ has a magnitude of 0.5 between $\eta=0.4\bar{w}$ and $\eta=0.6\bar{w}$, and 0.1 elsewhere. Other problem parameters are $Bi = 2$, $\gamma_1 = 0.5$, $\bar{w} = 2$, $\bar{k}_1 = 4$, $\bar{\alpha}_1 = 1.8$. The initial condition for this and all subsequent analyses presented in this Section is 1.0, unless specified otherwise. Fig. 2(a) presents a plot of temperature as a function of time at $\xi=0.75$ and $\eta=\bar{w}/2$ for multiple values of N. Similarly, Figs. 2(b) and 2(c) present temperature fields as functions of ξ and η, respectively, at $\tau=0.6$. In Fig. 2(b), $\eta=\bar{w}/2$, while in Figure 2(c), $\xi=0$. In each plot, convergence in the temperature profile is observed beyond $N = 15$, with the $N = 15$ and $N = 20$ curves being practically coincident. Therefore, a value of $N = 20$ is used for all subsequent analyses presented here, although it is noted that a greater number may be needed in case the temperature distribution is desired at very small times. In general, for any particular problem of interest, it is recommended to determine the acceptable value of N through convergence analysis.

4.2. Numerical validation

A comparison between the analytical solution presented here and finite-element based numerical simulations is carried out. For this purpose, numerical simulations are carried out in ANSYS-CFX, with a mesh count of around 16,000. Mesh independence and timestep convergence of the numerical model is ensured before the comparison. For a problem with the same parameters as Fig. 2, Fig. 3 presents a comparison between the present work and numerical simulations. Fig. 3(a) presents the temperature as a function of time at the midpoints of layers 1 and 2. At $\tau=0.1, 0.2, 0.6$ and 1.0, Fig. 3(b) plots temperature as a function of ξ at $\eta=\bar{w}/2$, whereas Fig. 3(c) plots temperature as a function of η at $\xi=0.25$. These plots show that the present analytical work agrees very well with numerical simulations, and is able to capture both spatial and transient variation of the temperature field. The worst-case error between the two is less than 1%.

Note that the theoretical technique developed here compares favorably with numerical simulations in terms of computational cost. Each temperature computation is found to take around 1.8 s on a four-core 2.8 GHz desktop computer. A numerical simulation takes at least tens of seconds, without even accounting for time taken for mesh generation. Another advantage of the theoretical technique is that temperature at any desired time can be directly calculated, whereas a numerical simulation typically must slowly march forward in time, starting from the initial time, thereby further increasing the computation cost. Finally, the theoretical results presented here can be easily implemented in a standard programming language and not need proprietary commercial software that numerical simulations often rely upon.

In addition to comparison with finite-element simulations, plots in Fig. 3 also highlight key features of the temperature field and its dependence on the heat flux and thermal contact resistance functions. For example, curves in Fig. 3(a) show that temperature in layer 1 begins to rise much more rapidly around $\tau=0.4$, which is in line with the switching of the heat load at that time. On the other hand, the temperature in layer 2 initially drops, and then starts to rise at $\tau=0.4$ as a result of the switching. The initial drop in the temperature of layer 2 is due to effective cooling at the $\xi=1$ boundary, coupled with shielding from the heat flux by the interfacial thermal contact resistance. In Fig. 3(b), it can be observed that temperature distribution in layer 1 keeps increasing with time. The change in the slope of the temperature distributions closer to the $\xi=0$ boundary at $\tau=0.6$ and $\tau=1.0$ essentially indicates switching
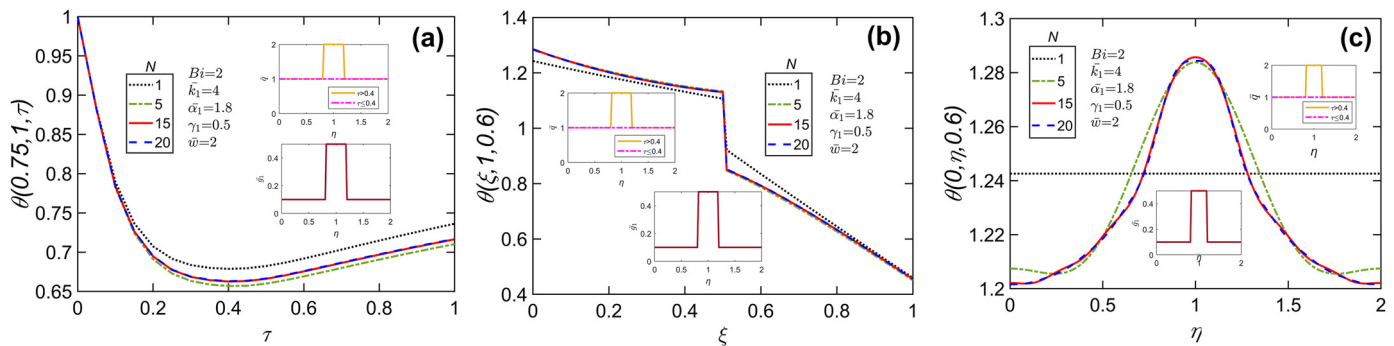
Fig. 2. Effect of N on temperature profiles: (a) θ as a function of τ at $\xi = 0.75$ and $\eta = \bar{w}/2$ for multiple number of eigenvalues; (b) θ as a function of ξ at $\tau = 0.6$ and $\eta = \bar{w}/2$ for multiple number of eigenvalues; (c) θ as a function of η at $\tau = 0.6$ and $\xi = 0$ for multiple number of eigenvalues. Problem parameters are $Bi = 2$, $\gamma_1 = 0.5$, $\bar{w} = 2$, $\bar{k}_1 = 4$, $\bar{\alpha}_1 = 1.8$. The heat flux $\bar{q}(\eta)$ is 1, when $\tau \leq 0.4$. The heat flux $\bar{q}(\eta)$ has a value of 2 between $\eta = 0.4\bar{w}$ and $\eta = 0.6\bar{w}$, and 1 elsewhere, when $\tau > 0.4$. Thermal contact resistance $\bar{g}_1(\eta)$ has a value of 0.5 between $\eta = 0.4\bar{w}$ and $\eta = 0.6\bar{w}$, and 0.1 elsewhere.

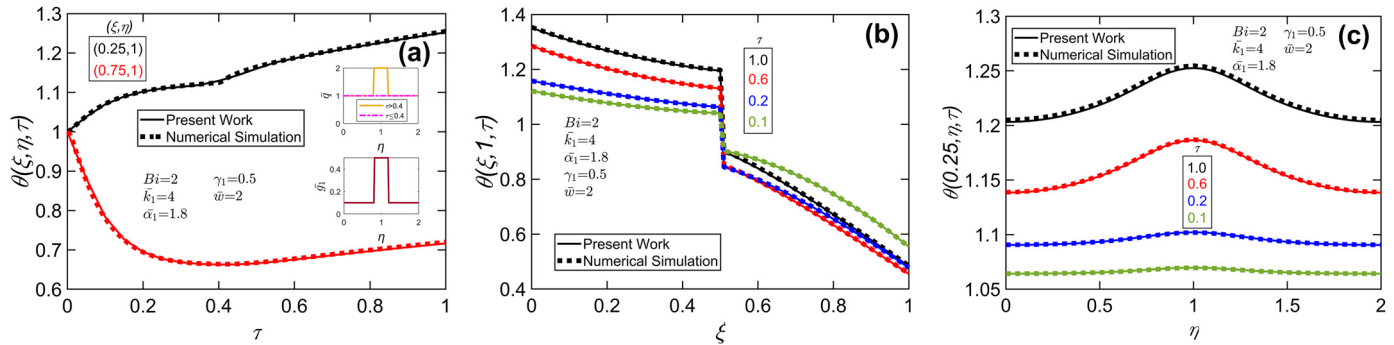**Fig. 3.** Numerical validation of present work: (a) θ as a function of τ at ($\xi = 0.25$, $\eta = \bar{w}/2$) and ($\xi = 0.75$, $\eta = \bar{w}/2$); (b) θ as a function of ξ at $\tau = 0.1$, 0.2, 0.6, 1 and $\eta = \bar{w}/2$ for multiple number of eigenvalues; (c) θ as a function of η at $\tau = 0.1$, 0.2, 0.6, 1 and $\xi = 0.25$ for multiple number of eigenvalues. Problem parameters, heat flux $\bar{q}(\eta)$ and thermal contact resistance $\bar{g}_1(\eta)$ are identical to Fig. 2.

of the heat load. The initial reduction in temperature in layer 2 can also be observed in the $\tau = 0.1$ and 0.2 curves in Fig. 3(b). Once the switching occurs, heat penetration into layer 2 begins to dominate, resulting in temperature rise in layer 2, as seen in the $\tau = 0.6$ and 1.0 curves. Fig. 3(c) shows a peak in the temperature distribution between $\eta = 0.4\overline{w}$ and $\eta = 0.6\overline{w}$ at $\xi = 0.25$ before switching, which is due to the spatially varying thermal contact resistance. After switching, the peak temperature in the same region is mainly impacted by the hotspot and thermal contact resistance. Further, the difference between the peak and minimum temperatures goes up, which is a direct effect of the hotspot caused by the increased heat flux.

4.3. Comparison with past work

The present work models a realistic heat dissipation scenario in a multilayer semiconductor device, and is capable of capturing the effects of a general, dynamically switching heat load, along with the presence of a spatially varying thermal contact resistance between the layers. It is helpful to compare the present work with results from a past paper that addressed the special case of steady state temperature distribution in a similar problem [15]. For the same heat load and thermal contact resistance distributions, results from the present work are expected to evolve with time and eventually align with the results from the past work at large times, when the system approaches steady state. To confirm this, the transient temperature field is computed using the present model, for parameter values consistent with the past work. Specifically, the heat flux $\bar{q}$ has values of 0.2 between $\eta = 0.4\bar{w}$ and $\eta = 0.6\bar{w}$, and 0.0 elsewhere. Thermal contact resistance has values of 0.5 be-

tween $\eta = 0.4\bar{w}$ and $\eta = 0.6\bar{w}$, and 0.1 elsewhere. The Biot number is $Bi = 1$ and the width is $\bar{w} = 5$, while all the other problem parameters are identical to Fig. 2. Temperature of layer 1 at ($\xi = 0.25$, $\eta = 0.2\bar{w}$) and ($\xi = 0.25$, $\eta = 0.5\bar{w}$) is presented as a function of time in Fig. 4(a). On the other hand, Fig. 4(b) presents temperature distribution along the η direction at $\xi = 0.25$ at various times. In addition to the time-varying curves from the present work, these Figures also present the corresponding steady state curves based on the past steady state work [15]. It can be seen in Fig. 4(a) that as time increases, the transient temperature profile computed from the present work correctly approaches the steady-state value for both locations considered here. Similarly, in Fig. 4(b), the temperature distribution is found to gradually decay and align well with the steady state temperature distribution at large time.

The good agreement between the computed transient temperature field at large field with independently computed steady state field is encouraging. A number of analyses based on the transient model are carried out next in order to study the nature of temperature field in the multilayer device, particularly the impact of various aspects of the heat load and thermal contact resistance functions.

4.5. Illustrative colorplots

Fig. 5 presents representative colorplots of the temperature field at multiple times for a representative problem, in which, the heat load initially has a magnitude of 5.0 between $\eta = 0.4\bar{w}$ and $\eta = 0.6\bar{w}$, and 1.0 everywhere else. Switching takes place at $\tau = 0.4$, when the heat load between $\eta = 0.4\bar{w}$ and $\eta = 0.6\bar{w}$ turns off, and increases everywhere else to a magnitude of 5.0. Such a change in the heat
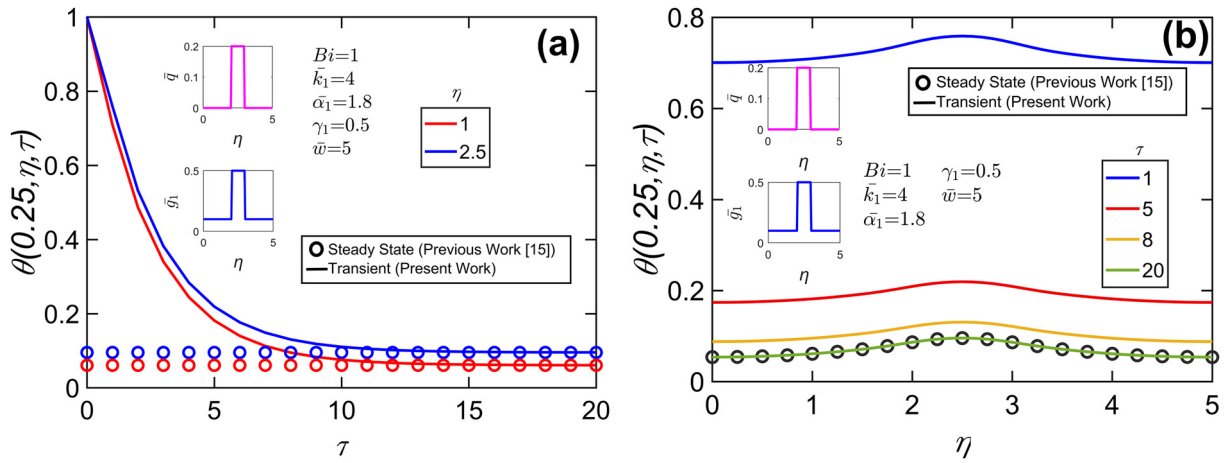
Fig. 4. Comparison with past work [15]: (a) θ as a function of τ at ($\xi = 0.25$, $\eta = 0.2\bar{w}$) and ($\xi = 0.25$, $\eta = \bar{w}/2$); (b) θ as a function of η at $\tau = 1$, 5, 8, 20 and $\xi = 0.25$. Problem parameters are $Bi = 1$, $\gamma_1 = 0.5$, $\bar{w} = 5$, $\bar{k}_1 = 4$, $\bar{\alpha}_1 = 1.8$. The heat flux $\bar{q}(\eta)$ has a value of 0.2 between $\eta = 0.4\bar{w}$ and $\eta = 0.6\bar{w}$, and zero elsewhere. Thermal contact resistance $\bar{g}_1(\eta)$ is identical to Fig. 2.
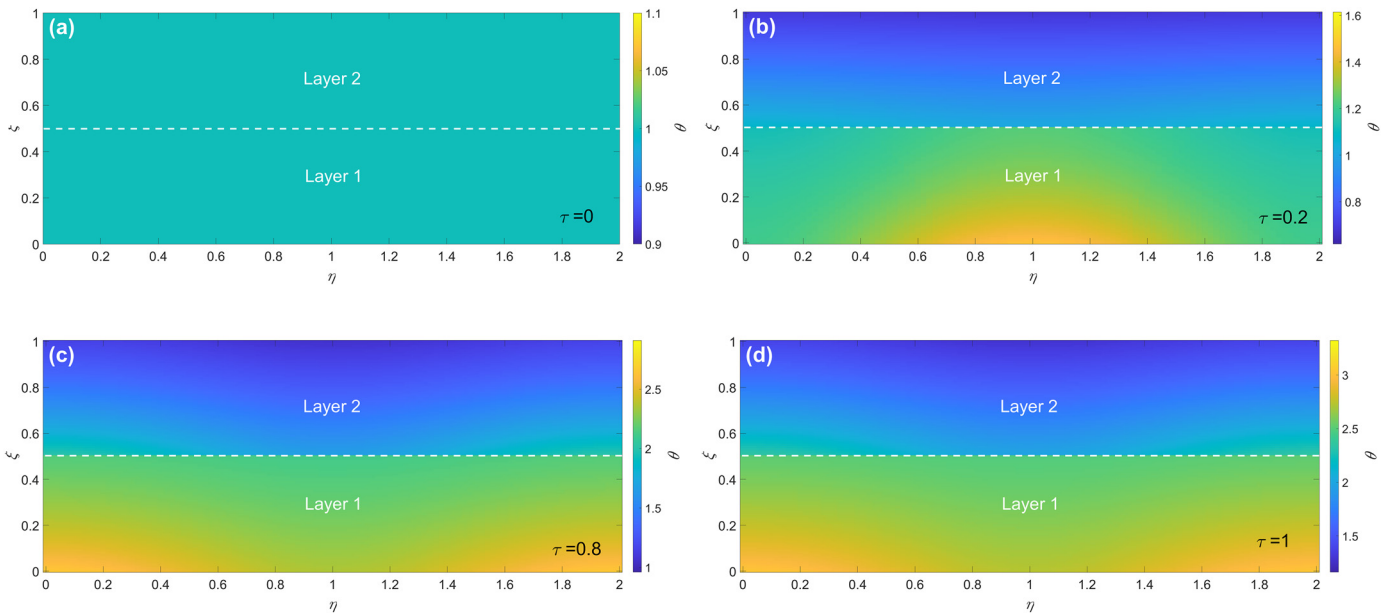
Fig. 5. Representative colorplots at: (a) $\tau = 0$; (b) $\tau = 0.2$; (c) $\tau = 0.8$; (d) $\tau = 1$. Problem parameters are $Bi = 1$, $\gamma_1 = 0.5$, $\bar{w} = 2$, $\bar{k}_1 = 4$, $\bar{\alpha}_1 = 1.8$. The heat flux $\bar{q}(\eta)$ is 5 between $\eta = 0.4\bar{w}$ and $\eta = 0.6\bar{w}$, and 1 elsewhere, when $\tau \leq 0.4$. The heat flux $\bar{q}(\eta)$ has a value of zero between $\eta = 0.4\bar{w}$ and $\eta = 0.6\bar{w}$, and 5 elsewhere, when $\tau > 0.4$. Thermal contact resistance $\bar{g}_1(\eta)$ is identical to Fig. 2.

load may model, for example, dynamic reallocation of computational workload that occurs commonly on multicore chips [28]. The Biot number is taken to be $Bi = 1$, while all other problem parameters, including the thermal contact resistance function are identical to Fig. 2. Fig. 5(b) shows a hotspot between $\eta = 0.4\bar{w}$ and $\eta = 0.6\bar{w}$ at $\xi = 0$, consistent with the heat flux profile. After the dynamic switching of heat load, the location of the hotspot is expected to change, and this is clearly captured in Fig. 5(c) and 5(d). As expected, the plots show two hotspots in line with heat flux profile after the switching. Additionally, the colorplots display heat penetration into layer 2 from the regions corresponding to the lower thermal contact resistance, as expected.

4.4. Effect of dynamic switching of heat load

For a representative two-layer problem, Fig. 6 presents the effect of dynamic switching of heat load on the temperature field. Temperature as a function of time at two locations 1A ($\xi = 0.4$, $\eta = 0.5\bar{w}$) and 1B ($\xi = 0.4$, $\eta = 0.2\bar{w}$) in layer 1 and at two locations 2A ($\xi = 0.75$, $\eta = 0.5\bar{w}$) and 2B ($\xi = 0.75$, $\eta = 0.2\bar{w}$) in layer 2 is plotted in Fig. 6(a), while temperature along the η direction at the heat flux face is plotted in Fig. 6(b). For this analysis, the problem parameters, including the heat flux and thermal contact resistance functions are identical to the ones used in Fig. 5.

Fig. 6(a) shows that the temperature profile at 1B is initially lower than the temperature profile at 1A, as expected. Once switching occurs at $\tau = 0.4$, temperature at 1B begins to rise rapidly and eventually crosses over the temperature curve for the other point. Furthermore, temperature rises at an increased rate at both points, but it must be noted that the 1B curve lies above the 1A curve, which is a direct consequence of the heat load switching. On the other hand, at both points in layer 2, the temperature initially drops due to cooling from the $\xi = 1$ boundary, followed by a rise at about the same rate until the switching. The rise in temperature after an initial drop is due to initial dominance of heat penetration from layer 1, followed by diffusion. Afterwards, temperature rise is slightly steeper at 2B than at 2A. This is attributable to the higher heat load around Point 2B coupled with a lower thermal
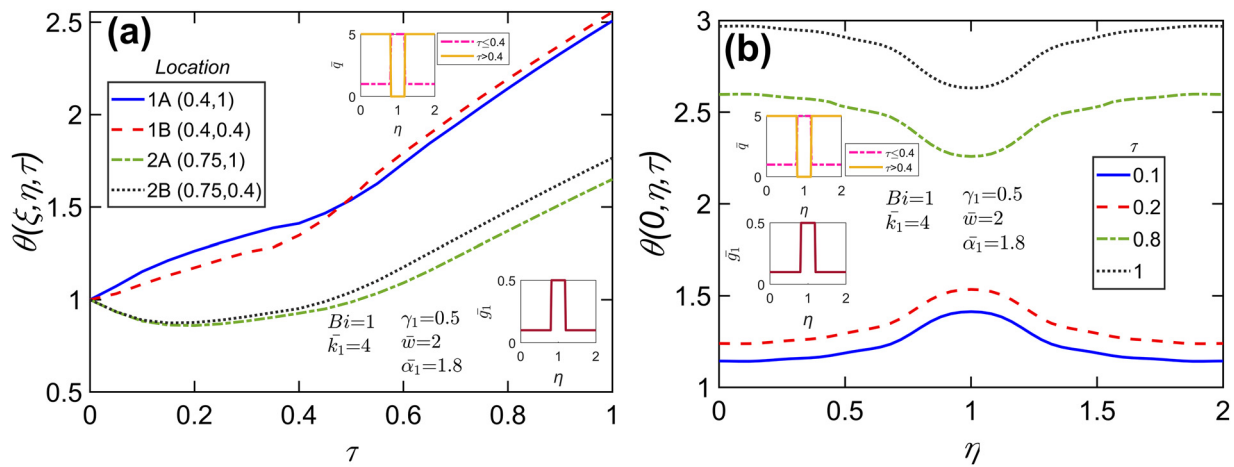
Fig. 6. Effect of dynamic heat load switching: (a) θ as a function of τ at $(\xi = 0.4, \eta = \bar{w}/2)$, $(\xi = 0.4, \eta = 0.2\bar{w})$, $(\xi = 0.75, \eta = \bar{w}/2)$ and $(\xi = 0.75, \eta = 0.2\bar{w})$; (b) θ as a function of η at $\tau = 0.1, 0.2, 0.8, 1$ and $\xi = 0$. Problem parameters, heat flux $\bar{q}(\eta)$ and thermal contact resistance $\bar{g}_1(\eta)$ are identical to Fig. 5.
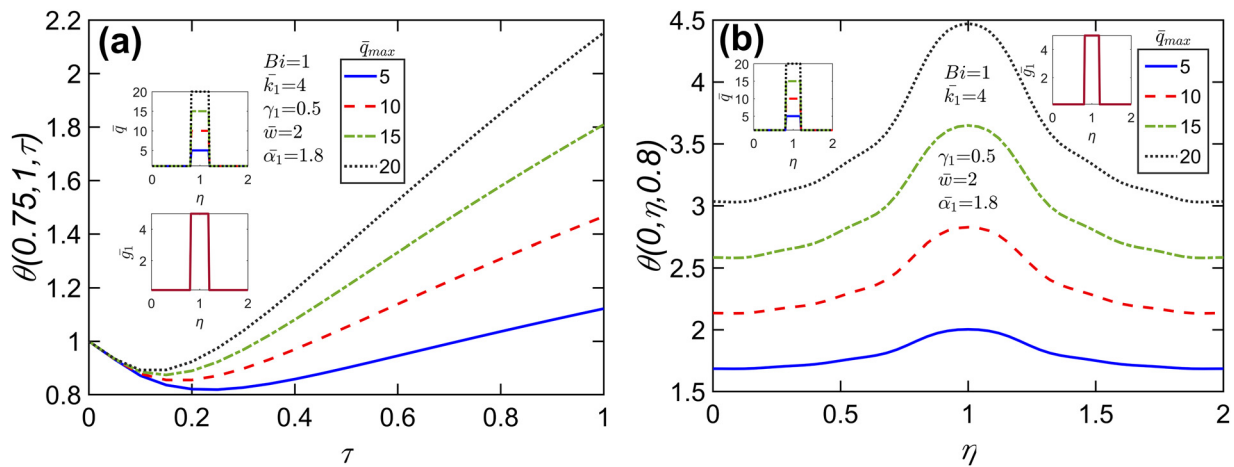

Fig. 7. Effect of peak heat flux: (a) θ as a function of τ at $\xi = 0.75$ and $\eta = \bar{w}/2$ for multiple values of $\bar{q}_{max}$; (b) θ as a function of η at $\tau = 0.8$ and $\xi = 0$ for multiple values of $\bar{q}_{max}$. Heat flux $\bar{q}(\eta)$ has a peak value of $\bar{q}_{max}$ between $\eta = 0.4\bar{w}$ and $\eta = 0.6\bar{w}$, and 1 elsewhere. Problem parameters are $Bi = 1$, $\gamma_1 = 0.5$, $\bar{w} = 2$, $\bar{k}_1 = 4$, $\bar{\alpha}_1 = 1.8$. Thermal contact resistance $\bar{g}_1(\eta)$ has a value of 5 between $\eta = 0.4\bar{w}$ and $\eta = 0.6\bar{w}$, and 0.1 elsewhere.

contact resistance. In Fig. 6(b), which presents temperature distribution along η at the heat flux face, the temperature distribution is found to keep rising, as expected, but there is also a switch in the peak temperature location. After the heat load turns off between $\eta = 0.4\bar{w}$ and $\eta = 0.6\bar{w}$, the temperature field dips in this region, and temperature everywhere else rises due to the increasing heat load.

4.6. Effect of peak heat flux

In order to investigate the effect of peak heat flux, the heat flux $\bar{q}$ is assumed to have a hotspot $\bar{q}_{max}$ between $\eta = 0.4\bar{w}$ and $\eta = 0.6\bar{w}$ and a value of 1.0 elsewhere. The temperature field is computed for multiple values of $\bar{q}_{max}$, while all other problem parameters are taken to be the same as Fig. 6. The thermal contact resistance also stays unchanged for all the cases with a magnitude of 5.0 between $\eta = 0.4\bar{w}$ and $\eta = 0.6\bar{w}$. Elsewhere along the interface, the contact resistance has a magnitude of 1. Fig. 7(a) plots temperature as a function of time at the midpoint of layer 2, while Fig. 7(b) plots temperature as a function of η at the heat flux face and at $\tau = 0.8$. Fig. 7(a) clearly shows, as expected, that the peak heat flux magnitude has a profound effect on the temperature profile even in layer 2. There exists a threshold time until which, the cooling coupled with thermal contact resistance shielding dominates the penetration of heat from layer 1. As $\bar{q}_{max}$ goes up, this threshold time is

found to go down. Further, the rate of temperature rise also goes up as the peak heat flux magnitude goes up. Similarly, Fig. 7(b) shows that the peak temperature goes up with increasing value of $\bar{q}_{max}$, as expected.

4.7. Effect of contact resistance magnitude and contact resistance interface location

Another important parameter of this multilayer device problem is the contact resistance, which is mainly characterized by its magnitude and location. Therefore, the impact of thermal contact resistance is analyzed in two parts.

The effect of the magnitude of the contact resistance is analyzed from the perspectives of both layers 1 and 2. Figs. 8(a) and 9(a) plot temperatures at the midpoints of layers 1 and 2, respectively, as functions of time. These plots are supplemented by temperature profiles along the η direction at $\tau = 0.8$ and at $\xi = 0$ and $\xi = 0.6$ in Figs. 8(b) and 9(b), respectively. The heat flux is $\bar{q} = 20$ between $\eta = 0.4\bar{w}$ and $\eta = 0.6\bar{w}$, and $\bar{q} = 1$ elsewhere. The contact resistance $\bar{g}_1$ is a top hat function as shown in the inset. All other problem parameters for this analysis are identical to the ones used in Fig. 6. Cases associated with $\bar{g}_{1,max} = 1, 5, 20$ and 100 are presented in Figs. 8 and 9. These plots clearly show that the effect of the contact resistance magnitude is stronger in layer 2 than layer 1. Fig. 9(a) shows that the threshold time at which temperature in
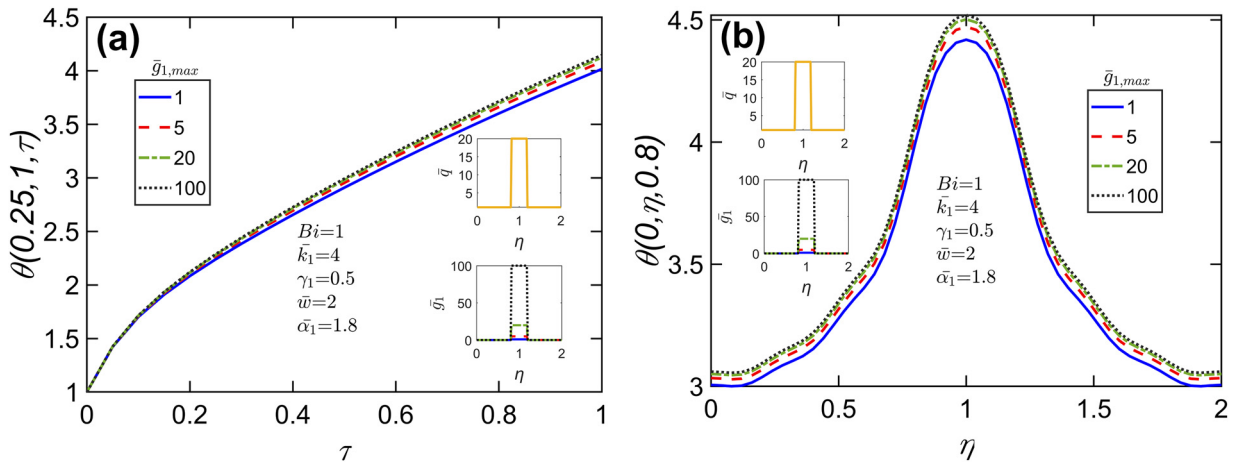
Fig. 8. Effect of peak contact resistance in layer 1: (a) θ as a function of τ at $\xi = 0.25$ and $\eta = \bar{w}/2$ for multiple values of $\bar{g}_{1,max}$; (b) θ as a function of η at $\tau = 0.8$ and $\xi = 0$ for multiple values of $\bar{g}_{1,max}$. Problem parameters, heat flux $\bar{q}(\eta)$ and thermal contact resistance $\bar{g}_1(\eta)$ are identical to Fig. 9.
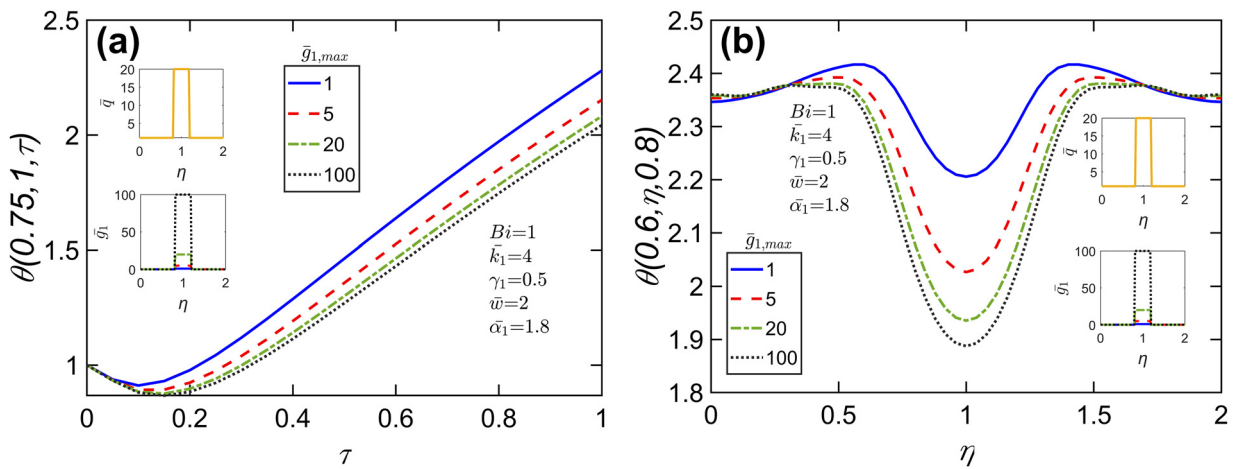

Fig. 9. Effect of peak contact resistance in layer 2: (a) θ as a function of τ at $\xi = 0.75$ and $\eta = \bar{w}/2$ for multiple values of $\bar{g}_{1,max}$; (b) θ as a function of η at $\tau = 0.8$ and $\xi = 0.6$ for multiple values of $\bar{g}_{1,max}$. Thermal contact resistance $\bar{g}_1(\eta)$ has a peak value of $\bar{g}_{1,max}$ between $\eta = 0.4\bar{w}$ and $\eta = 0.6\bar{w}$, and 0.1 elsewhere. Problem parameters are $Bi = 1$, $\gamma_1 = 0.5$, $\bar{w} = 2$, $\bar{k}_1 = 4$, $\bar{\alpha}_1 = 1.8$. The heat flux $\bar{q}(\eta)$ has a value of 20 between $\eta = 0.4\bar{w}$ and $\eta = 0.6\bar{w}$, and 1 elsewhere.

layer 2 starts to rise goes up as $\bar{g}_{1,max}$ increases. Moreover, beyond a certain value of $\bar{g}_{1,max}$, the shielding effect seems to be significantly weakened. This is because beyond a certain value of $\bar{g}_{1,max}$, most of the heat is able to diffuse into layer 2 only through regions with lower contact resistance. An increase in the value of $\bar{g}_{1,max}$ beyond this point will result in nearly zero heat flux through the region corresponding to $\bar{g}_{1,max}$, which is an indication of extremely large contact resistance. The shielding effect of contact resistance is also seen in Fig. 9(b). As $\bar{g}_{1,max}$ increases, the minimum temperature along the η direction reduces proportionally. Similar to Fig. 9(a), however, the reduction is less and less significant as $\bar{g}_{1,max}$ increases. Increase in $\bar{g}_{1,max}$ is expected to raise the temperature of layer 1 region associated with $\bar{g}_{1,max}$ due to an increase in heat flow obstruction by the thermal contact resistance. Based on this, the temperature profiles in Fig. 8(a) and 8(b) are found to shift slightly upwards as $\bar{g}_{1,max}$ goes up.

As the shift in the observed peak temperature at the heat flux face with an increase in $\bar{g}_{1,max}$ is not very significant, the effect of the relative thickness of the two layers, as represented by the non-dimensional parameter γ_1 is studied in Fig. 10(a) and 10(b). The analysis is carried out by plotting temperature as a function of η at the heat flux face and at $\tau = 0.8$ for multiple values of γ_1. In both figures, the heat flux profile and other problem parameters used are identical to the ones used in Figs. 8 and 9. In Fig. 10(a), the thermal contact resistance is $\bar{g}_1 = 0.5$ between $\eta = 0.4\bar{w}$ and $\eta = 0.6\bar{w}$,

whereas in Fig. 10(b), $\bar{g}_1 = 100$ between $\eta = 0.4\bar{w}$ and $\eta = 0.6\bar{w}$. In both cases, the contact resistance has a magnitude of 0.1 elsewhere. Figs. 10(a) and 10(b) show that the peak temperature shifts up significantly as the contact resistance interface is brought closer to the heat flux face. The shift in case (b) is greater than in case (a), as expected, due to a higher contact resistance magnitude. Therefore, it can be concluded that the distance between the contact resistance interface and heat flux face plays a key role on the peak temperature. However, one must also consider that the significant shift in peak temperature is due to a reduction in the amount of material available for heat diffusion in layer 1.

4.8. Effect of Biot number

Finally, the effect of Biot number is analyzed by computing temperature as a function of time at the midpoint of layer 2. Fig. 11 presents these plots for two specific cases. In the first case, $\bar{q}_{max}$ and $\bar{g}_{1,max}$ values are 0.2 and 0.5, respectively, whereas in the second case $\bar{q}_{max}$ and $\bar{g}_{1,max}$ are much larger, 20 and 100, respectively. In both the cases, $\bar{g}_{1,max}$ and $\bar{q}_{max}$ are between $\eta = 0.4\bar{w}$ and $\eta = 0.6\bar{w}$. The heat flux $\bar{q}$ is zero everywhere else in the first case, whereas $\bar{q}$ is 1.0 everywhere else in the second case. On the other hand, $\bar{g}_1 = 0.1$ everywhere else in both cases. Other problem parameters are identical to that of Fig. 8. The strong impact of Biot number on the temperature profiles is evident from Fig. 11(a) and 11(b).
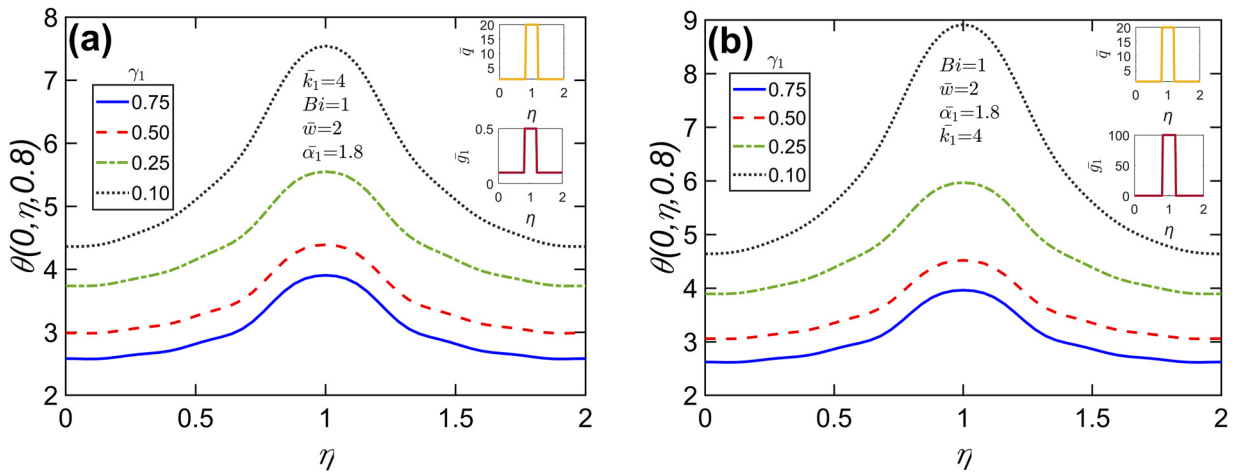
Fig. 10. Effect of interface location on peak temperature: (a) θ as a function of η at $\tau = 0.8$, $\xi = 0$ for multiple values of γ_1 and $\bar{g}_{1,max} = 0.5$; (b) θ as a function of η at $\tau = 0.8$, $\xi = 0$ for multiple values of γ_1 and $\bar{g}_{1,max} = 100$. Thermal contact resistance $\bar{g}_1(\eta)$ has a peak value of $\bar{g}_{1,max}$ between $\eta = 0.4\bar{w}$ and $\eta = 0.6\bar{w}$, and 0.1 elsewhere. The heat flux $\bar{q}(\eta)$ is 20 between $\eta = 0.4\bar{w}$ and $\eta = 0.6\bar{w}$, and 1 elsewhere. Problem parameters are identical Fig. 9.
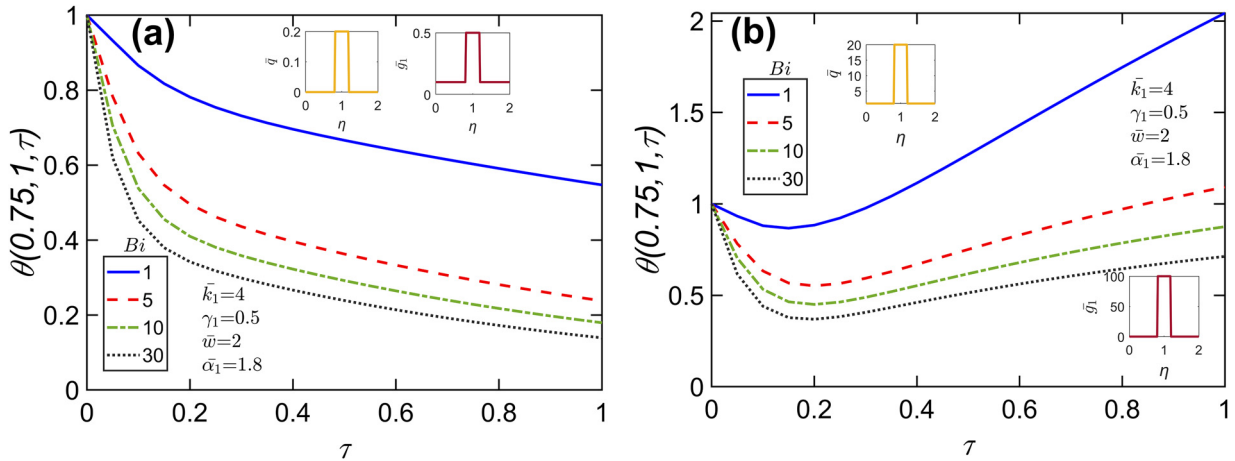

Fig. 11. Effect of Biot number: (a) θ as a function of τ at $\xi = 0.75$, $\eta = \bar{w}/2$ for multiple values of Bi, $\bar{g}_{1,max} = 0.5$, $\bar{q}_{max} = 0.2$, $\bar{g}_{1,min} = 0.1$ and $\bar{q}_{min} = 0$; (b) θ as a function of τ at $\xi = 0.75$, $\eta = \bar{w}/2$ for multiple values of Bi, $\bar{g}_{1,max} = 100$, $\bar{q}_{max} = 20$, $\bar{g}_{1,min} = 0.1$ and $\bar{q}_{min} = 1$. Heat flux $\bar{q}(\eta)$ and thermal contact resistance $\bar{g}_1(\eta)$ have a peak value of $\bar{q}_{max}$ and $\bar{g}_{1,max}$ between $\eta = 0.4\bar{w}$ and $\eta = 0.6\bar{w}$, respectively. For case (a) and case (b), $\bar{q}(\eta)$ and $\bar{g}_1(\eta)$ are equal to $\bar{g}_{1,min}$ and $\bar{q}_{min}$ elsewhere, respectively. Problem parameters are $\gamma_1 = 0.5$, $\bar{w} = 2$, $\bar{k}_1 = 4$, $\bar{\alpha}_1 = 1.8$.

For example, in Fig. 11(a), as the Biot number increases, the overall rate of cooling goes up, with a particularly significant jump between $Bi=1$ and $Bi=5$. Beyond $Bi=5$, there is only a slight change in the overall rate of cooling, which is likely because $Bi=5$ is close to the limiting isothermal condition. In each case, the initial drop in temperature is heavily dictated by the magnitude of the Biot number until a certain time. This initial drop in temperature is particularly significant for a large Biot number, due to more effective cooling. This effect corresponds to the time taken from heat to diffuse from layer 1 to the midpoint of layer 2. Afterwards, the rate of cooling reduces and then remains nearly constant. On the other hand, in Fig. 11(b), due to the larger magnitude of heat flux and contact resistance, the temperature initially drops and then rises for each case. As the Biot number is increased, the cooling is enhanced, as expected. Also, the threshold time for which the cooling dominates heat penetration from layer 1 goes up, as Biot number is increased.

4.9. Illustration with a practical problem

The capability of the theoretical model developed here is illustrated by solving a practical problem of thermal transport in a heterogeneously integrated two-die stack comprising Si and Si/Ge substrates of thickness 1 mm each and width 10 mm. The interest is in determining the peak temperature rise in response to a heating pulse of magnitude 400 W/cm^2 lasting 0.4 s. Two locations of the heating pulse at one end are considered, as illustrated in the inset of Fig. 12 – between $x = 1.0$ mm and $x = 1.5$ mm (Case A) and between $x = 4.5$ mm and $x = 5.0$ mm (Case B). The convective heat transfer coefficient at the other end is 200 Wm^{-2}K^{-1}. In each case, the thermal contact resistance between the two layers is 5.0 μKm^{2}W^{-1} between $x = 4.0$ mm and $x = 6.0$ mm, and 1000 μKm^{2}W^{-1} elsewhere, which represents a significant increase in interfacial conduction in the middle region due to the presence of high-density TSVs. The ambient as well as the initial temperature is taken to be 298 K, and the interest is in determining the peak temperature rise in both cases. Results are plotted in Fig. 12 in terms of peak temperature as a function of time. It is found that Case A incurs greater temperature rise than Case B, which may be due to increased two-dimensionality of heat flow in Case A, due to non-alignment between the heat source and the low resistance region at the interface. This results in additional thermal spreading resistance. In contrast, heat flow is a lot more one-dimensional in Case B, which, as a result has relatively lower temperature rise. This plot illustrates the capability of the theoretical model developed to solve practical thermal design problems that are not solv-
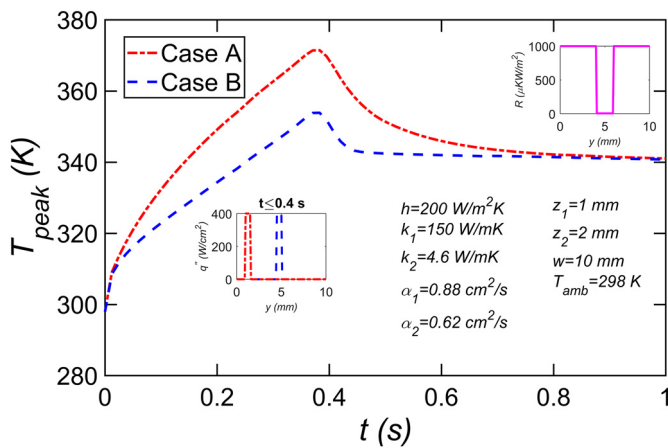
Fig. 12. Peak temperature as a function of time for a practical two-layer 3D IC problem comprising Si and Si/Ge substrates. Two different heat flux distributions are considered, for which, the parameter values are listed in Section 4.9. Inset plots illustrate the heat flux distributions as well as the thermal contact resistance distribution between the two layers.

able using past work, such as papers that solve steady state problems [15].

5. Conclusions

The key contribution of this work is a robust analytical thermal model capable of accounting for complex, realistic phenomena that occur in practical multilayer semiconductor devices such as 3D ICs. A dynamically switching and spatially varying heat load, as well as a spatially varying interfacial thermal contact resistance are modeled. The analytical model presented in this work generalizes much of the past work, where the contact resistance is either modeled as a constant or is absent altogether. This model may help correctly predict the dynamic thermal performance of 3D ICs under realistic load conditions. The modeling framework presented here is equally applicable for other multilayer problems in semiconductor thermal management, such as a multilayer heat spreader on top of a microelectronics chip.

While presented in the context of a two-dimensional problem, extension to a 3D problem is quite straightforward, and will involve an additional set of eigenfunctions. Realistic heat loads based on power maps from actual 3D ICs may be easily implemented in order to predict the thermal performance of the 3D IC.

Declaration of Competing Interest

None.

CRediT authorship contribution statement

Girish Krishnan: Conceptualization, Methodology, Formal analysis, Validation, Investigation, Data curation, Writing – original draft, Writing – review & editing. **Ankur Jain:** Conceptualization, Methodology, Formal analysis, Project administration, Writing – original draft, Writing – review & editing.

Data availability

Data will be made available on request.

References

[1] S.S. Salvi, A. Jain, A review of recent research on heat transfer in three-dimensional integrated circuits (3-D ICs), IEEE Trans. Components Pack. Manuf. Technol. 11 (2021) 802–821, doi:10.1109/TCPMT.2021.3064030.

[2] R. Mahajan, C.P. Chiu, G. Chrysler, Cooling a microprocessor chip, Proc. IEEE. 94 (2006) 1476–1485, doi:10.1109/JPROC.2006.879800.

[3] A. Bar-Cohen, Thermal management of microelectronics in the 21st century, in: Proceedings of the IEEE EPTC, 1997, pp. 29–33, doi:10.1109/EPTC.1997.723880.

[4] S.V. Garimella, Y.K. Joshi, A. Bar-Cohen, R. Mahajan, K.C. Toh, V.P. Carey, M. Baelmans, J. Lohan, B. Sammakia, F. Andros, Thermal challenges in next generation electronic systems- summary of panel presentations and discussions, in: Proceedings of the IEEE Transactions on Components and Packaging Technologies, 2002, pp. 569–575, doi:10.1109/TCAPT.2003.809113.

[5] D.B. Tuckerman, R.F.W. Pease, High-performance heat sinking for VLSI, *IEEE Electron Dev. Lett.* EDL 2 (1981) 126–129, doi:10.1109/EDL.1981.25367.

[6] S.M. Jayantha, G. McVicker, K. Bernstein, J.U. Knickerbocker, Thermomechanical modeling of 3D electronic packages, IBM J. Res. Develop. 52 (2008) 623–634, doi:10.1147/JRD.2008.5388568.

[7] M.S. El-Genk, Immersion cooling nucleate boiling of high power computer chips, Energy Convers Manag. 53 (2012) 205–218, doi:10.1016/j.enconman.2011.08.008.

[8] A.L. Moore, L. Shi, Emerging challenges and materials for thermal management of electronics, Mater. Today 17 (2014) 163–174, doi:10.1016/j.mattod.2014.04.003.

[9] S.G. Kandlikar, Review and projections of integrated cooling systems for three-dimensional integrated circuits, J. Electron. Packag. (2014) 136, doi:10.1115/1.4027175.

[10] V. Venkatadri, B. Sammakia, K. Srihari, D. Santos, A review of recent advances in thermal management in three dimensional chip stacks in electronic systems, J. Electron. Packag. (2011) 133, doi:10.1115/1.4005298.

[11] Y. Zhang, Y. Zhang, M.S. Bakir, Thermal design and constraints for heterogeneous integrated chip stacks and isolation technology using air gap and thermal bridge, IEEE Trans. Compon. Pack. Manuf. Technol. 4 (2014) 1914–1924, doi:10.1109/TCPMT.2014.2364742.

[12] J.H. Lau, T.G. Yue, Thermal management of 3D IC integration with TSV (Through silicon via), in: Proceedings of the IEEE ECTC, 2009, pp. 624–640, doi:10.1109/ECTC.2009.5074080.

[13] Y. Zhang, A. Dembla, M.S. Bakir, Silicon micropin-fin heat sink with integrated TSVs for 3-D ICs: tradeoff analysis and experimental testing, IEEE Trans. Compon. Pack. Manuf. Technol. 3 (2013) 1842–1850, doi:10.1109/TCPMT.2013.2267492.

[14] L. Choobineh, A. Jain, Determination of temperature distribution in three-dimensional integrated circuits (3D ICs) with unequally-sized die, Appl. Therm. Eng. 56 (2013) 176–184, doi:10.1016/j.applthermaleng.2013.03.006.

[15] G. Krishnan, A. Jain, Heat transfer in a multi-layered semiconductor device with spatially-varying thermal contact resistance between layers, Int. Commmunic. Heat Mass Transf. 140 (2023), doi:10.1016/j.icheatmasstransfer.2022.106482.

[16] L. Choobineh, A. Jain, An explicit analytical model for rapid computation of temperature field in a three-dimensional integrated circuit (3D IC), Int. J. Thermal Sci. 87 (2015) 103–109, doi:10.1016/j.ijthermalsci.2014.08.012.

[17] L. Choobineh, J. Jones, A. Jain, Experimental and numerical investigation of interdie thermal resistance in three-dimensional integrated circuits, J. Electronic Packag. (2017) 139, doi:10.1115/1.4036404.

[18] W. Huang, K. Sankaranarayanan, K. Skadron, R.J. Ribando, M.R. Stan, Accurate, pre-RTL temperature-aware design using a parameterized, geometric thermal model, IEEE Trans. Comput. 57 (2008) 1277–1288, doi:10.1109/TC.2008.64.

[19] Y. Zhang, C.R. King, J. Zaveri, Y.J. Kim, V. Sahu, Y. Joshi, M.S. Bakir, Coupled electrical and thermal 3D IC centric microfluidic heat sink design and technology, in: Proceedings of the IEEE ECTC, 2011, pp. 2037–2044, doi:10.1109/ECTC.2011.5898797.

[20] W.L. Hung, G.M. Link, Y. Xie, N. Vijaykrishnan, M.J. Irwin, Interconnect and thermal-aware floorplanning for 3D microprocessors, in: Proceedings of the IEEE ISQED, 2006, pp. 98–104, doi:10.1109/ISQED.2006.77.

[21] A. Jain, S.M. Alam, S. Pozder, R.E. Jones, Thermal–electrical co-optimisation of floorplanning of three-dimensional integrated circuits under manufacturing and physical design constraints, IET Comput. Digit. Techniq. 5 (2011) 169–178, doi:10.1049/iet-cdt.2009.0107.

[22] J. Cong, G. Luo, Y. Shi, Thermal-aware cell and through-silicon-via co-placement for 3D ICs, in: Proceedings of the ACM DAC, 2011, pp. 670–675, doi:10.1145/2024724.2024876.

[23] T. Zhang, Y. Zhan, S.S. Sapatnekar, Temperature-aware routing in 3D ICs, in: Proceedings of the IEEE ASPDAC, 2006, pp. 309–314, doi:10.1145/1118299.1118377.

[24] G.L. Loi, B. Agrawal, N. Srivastava, S.-C. Lin, T. Sherwood, K. Banerjee, A thermally-aware performance analysis of vertically integrated (3-D) processor-memory hierarchy, in: Proceedings of the ACM DAC, 2006, pp. 991–996, doi:10.1145/1146909.1147160.

[25] K.H. Lu, S.K. Ryu, J. Im, R. Huang, P.S. Ho, Thermomechanical reliability of through-silicon vias in 3D interconnects, in: Proceedings of the IEEE IRPS, 2011, doi:10.1109/IRPS.2011.5784487.

[26] A. Jain, R.E. Jones, R. Chatterjee, S. Pozder, Analytical and numerical modeling of the thermal performance of three-dimensional integrated circuits, IEEE Trans. Components Pack. Technol. 33 (2010) 56–63, doi:10.1109/TCAPT.2009.2020916.

[27] A. Jain, S.M. Alam, S. Pozder, R.E. Jones, Thermal-electrical co-optimisation of floorplanning of three-dimensional integrated circuits under manufacturing and physical design constraints, IET Comput. Digit. Tech. 5 (2011) 169–178, doi:10.1049/iet-cdt.2009.0107.

[28] S.H. Pan, N. Chang, T. Hitomi, 3D-IC dynamic thermal analysis with hierarchical and configurable chip thermal model, in: *Proceedings of the* IEEE 3D IC Conference, 2013, doi:10.1109/3DIC.2013.6702373.

[29] S. Pozder, A. Jain, R. Chatterjee, Z. Huang, R.E. Jones, E. Acosta, B. Marlin, G. Hillmann, M. Sobczak, G. Kreindl, S. Kanagavel, H. Kostner, S. Pargfrieder, 3D Die-to-wafer Cu/Sn microconnects formed simultaneously with an adhesive dielectric bond using thermal compression bonding, in: *Proc. IEEE Int. Interconnect Technol. Conf.*, 2008, pp. 46–48, doi:10.1109/IITC.2008.4546921.

[30] Z. Huang, R.E. Jones, A. Jain, Experimental investigation of electromigration failure in Cu-Sn-Cu micropads in 3D integrated circuits, Microelectron. Eng. 122 (2014) 46–51, doi:10.1016/j.mee.2014.03.003.

[31] E.G. Colgan, P. Andry, B. Dang, J.H. Magerlein, J. Maria, R.J. Polastre, J. Wakil, Measurement of microbump thermal resistance in 3D chip stacks, in: *Proceedings of the* IEEE SEMI-THERM, 2012, pp. 1–7, doi:10.1109/STHERM.2012.6188818.

[32] L. Zhou, M. Parhizi, A. Jain, Theoretical modeling of heat transfer in a multilayer rectangular body with spatially-varying convective heat transfer bound-ary condition, Int. J. Therm. Sci. 170 (2021) 107156, doi:10.1016/j.ijthermalsci.2021.107156.

[33] G. Krishnan, A. Jain, Theoretical analysis of a two-dimensional multilayer diffusion problem with general convective boundary conditions normal to the layered direction, Int. J. Heat Mass Transf. 202 (2023) 123723, doi:10.1016/j.ijheatmasstransfer.2022.123723.

[34] K.J. Hollenbeck, 'INVLAP.M: a matlab function for numerical inversion of Laplace transforms by the de Hoog algorithm,' available at http://www.isva.dtu.dk/staff/karl/invlap.htm.accessed.1/1/2012.

[35] A. Talbot, The accurate numerical inversion of Laplace transforms, IMA J. *Appl. Math.* 23 (1979) 97–120, doi:10.1093/imamat/23.1.97.

[36] L.N. Trefethen, J.A.C. Weideman, T. Schmelzer, Talbot quadratures and rational approximations, BIT Numer. *Math.* 46 (2006) 653–670, doi:10.1007/s10543-006-0077-9.